Pergamon

Int. J. Heat Mass Transfer. Vol. 39, No. 1, pp. 149–164, 1996

0017–9310/96 $9.50 + 0.00

0017–9310(95)00094–1

Investigation of flow and heat transfer in corrugated passages—I. Experimental results

J. STASIEK, M. W. COLLINS

Thermofluids Engineering Research Centre, City University, Northampton Square, London EC1V 0HB, U.K.

M. CIOFALO

Dipartimento di Ingegneria Nucleare, Università di Palermo Viale delle Scienze, 90128 Palermo, Italy

and

P. E. CHEW

PowerGen plc, Power Technology Centre, Ratcliffe-on-Soar, Nottingham NG11 0EE, U.K.

(*Received* 23 *July* 1993 *and in final form* 9 *February* 1995)

Abstract—An experimental and numerical study of flow and heat transfer was conducted for a crossed-corrugated geometry, representative of compact heat exchangers including air preheaters for fossil-fuelled power plant. In this paper, we describe the method of applying thermochromic liquid crystals and true-colour image processing to give local Nusselt number distribution over the surface, and average Nu, both of quantitative reliability; a careful uncertainty analysis is also presented. Typical experimental results for heat transfer and pressure drop are presented and discussed for various geometries and Reynolds numbers, and are compared with literature data. Numerical predictions are discussed in Part II.

1. INTRODUCTION

1.1. *Rotary air preheaters*

Compact heat exchangers are found in almost every field of engineering, from energy production to transport technology [1]. In particular, air heaters are essential components of fossil-fuelled power plant [2, 3]. Typically, they cool the flue gases leaving the final water-heating stage (economizer) from ~300 to ~100°C, and deliver warm air at ~250°C to the furnace. In a 500 MWe unit, air heaters may recover some 100 MW of low-grade heat, thus contributing substantially to the overall efficiency of the plant; moreover, preheating the combustion air makes the use of lower-grade fuels possible and, in coal-fired plant, provides the means of drying the fuel.

Air heaters can be classified into surface-type exchangers, or recuperators, and storage-type exchangers, or regenerators. The latter are cheaper, more compact and less sensitive to corrosion and fouling, and thus are invariably preferred in large power plant.

Rotary regenerators rely on the heat storage capacity of a matrix of closely packed corrugated steel plates, alternately exposed to the hot flue gases and to the cool combustion air. In the Ljungstrøm design, the matrix rotates between stationary ducts; in the Rothemühle design the matrix is stationary and rotating hoods distribute the two streams through it (Fig. 1). The two designs are essentially equivalent; the heat storage matrix is built in the form of a squat cylinder, typically having a vertical axis, with a diameter of ~10 m and a depth of ~2 m. Two such units serve a 500 MWe boiler; each of them is crossed by flue gases/air flow rates of about 200 $m^3 s^{-1}$, with an average speed of 3–6 m s^{-1}. The surface-to-volume ratio may be as high as 5–600 $m^2 m^{-3}$.

The theory of rotary regenerators dates back to Nusselt [4] and has been extended, for example, by Hausen [5]; computer simulations of the overall behaviour of regenerators appeared as early as the late 1960s [6], and design criteria are discussed in handbooks such as ref. [1]. However, the models used in the above and similar works assume that convective heat transfer coefficients are somehow known, while the optimum design of these devices requires knowledge of heat transfer coefficients and friction factors, and of their dependence on the corrugation geometry and on the Reynolds numbers.

The main features of performance required of an air heater are high heat transfer rates, low pressure losses and low sensitivity to fouling. These depend crucially on the geometrical design of the heat transfer elements. Several arrangements have been used in the

NOMENCLATURE

A_c	cross-section of unitary cell [m^2]
Δa	length of unitary cell [m]
D_{eq}	hydraulic diameter, $4S/V$ [m]
f	equivalent friction coefficient, see equation (6)
F	velocity peaking factor
G	mass flow rate in unitary cell [kg s^{-1}]
h	convective heat transfer coefficient [W m^{-2} K^{-1}]
H	total (external) height of corrugations [m]
H_i	internal height of corrugations [m]
j	Colburn factor, $Nu\ Re^{-1}\ Pr^{-1/2}$ or $Sh\ Re^{-1}\ Sc^{-1/2}$
L	auxiliary length, see Table 1 [m]
Nu	local Nusselt number, see equation (7)
$\langle Nu \rangle$, Nu_{av}	average Nusselt number, see equations (8) and (9)
P	pitch of corrugations [m]
Δp	pressure drop in unitary cell [Pa]
Pr	Prandtl number
q	heat flux [W m^{-2}]
Re	Reynolds number, see equation (5)
s	plate thickness [m]
S	surface area of unitary cell [m^2]
Sc	Schmidt number
Sh	Sherwood number
T	temperature [K]
U	mean velocity [m s^{-1}]
V	internal volume of unitary cell [m^3]
x_i	generic variable.

Greek symbols

α	auxiliary angle, see equations (1)–(3)
δ	thickness [m]
ε	uncertainty
θ	included angle between corrugations
λ	thermal conductivity [W m^{-1} K^{-1}]
ρ	density [kg m^{-3}]
ϕ, ϕ'	auxiliary angles, see equation (2).

Subscripts

b	thermo-static bath
f	fluid (air)
t	plate
w	wall.

past, differing in the shape and size of the corrugations formed by the steel plates; some of them are shown in Fig. 2 [3].

The various corrugation designs have been developed so far mainly on an empirical basis. Although both operating and laboratory data are available, they do not cover the full range of shapes, sizes and operating conditions (in particular, Reynolds numbers) that would be required for an optimization study; moreover, data are generally available in the form of overall performance (average heat transfer coefficient, pressure drop), and the phenomena which determine these (including flow patterns and transition to turbulence) are not fully understood.

On the basis of the above considerations, a comprehensive experimental and predictive research pro-

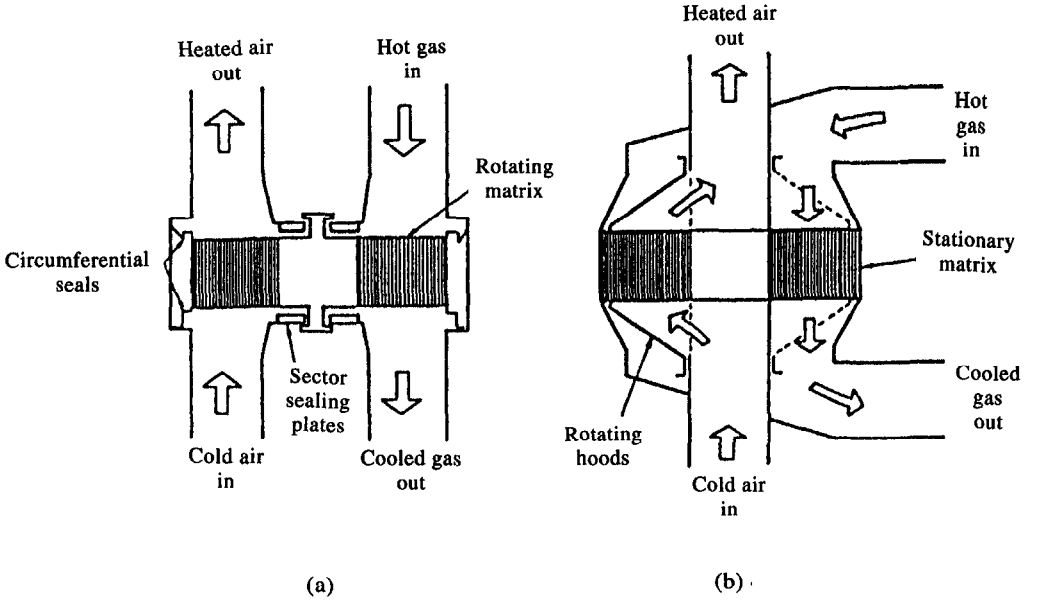

Fig. 1. Schematic of rotary air preheaters. (a) Ljungstrøm design; (b) Rothemühle design.

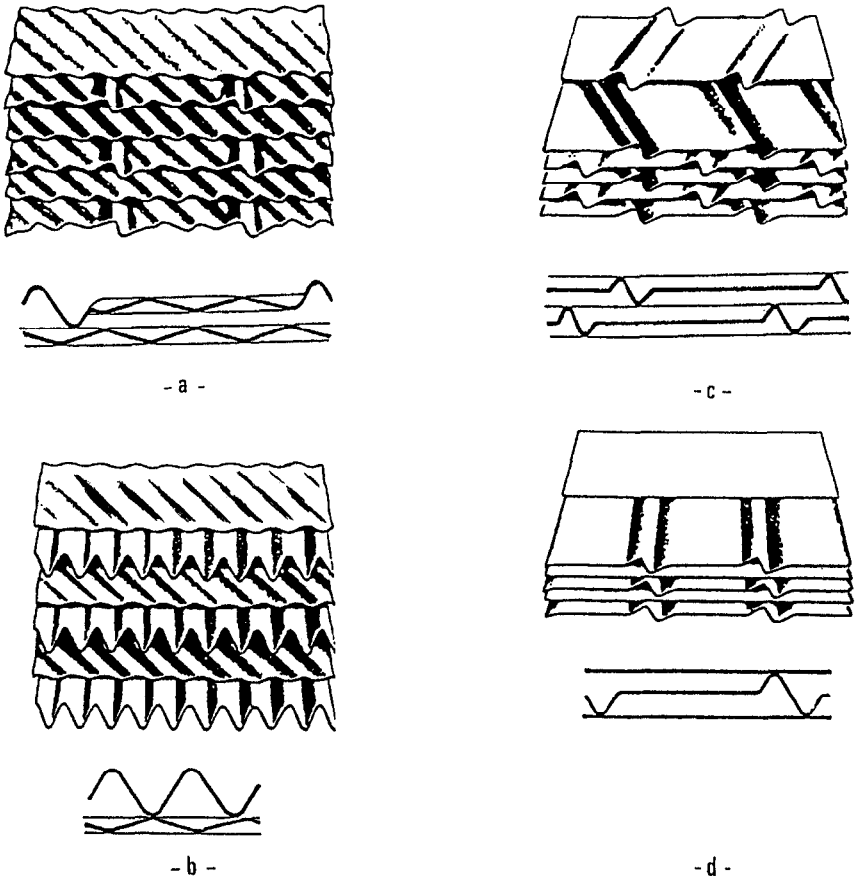

Fig. 2. Alternative corrugation designs for rotary air preheaters. (a) Double undulated (DU); (b) corrugated undulated (CU); (c) flat notched crossed (FNC); (d) notched plain (NP).

gram has been carried out by the authors and their colleagues with the industrial sponsorship of Power-Gen plc, U.K. The main purposes of the study were as follows.

(1) To investigate the dependence of heat transfer and pressure drop on Reynolds number and geometrical parameters, by making these vary in a systematic way and in sufficiently broad range. This was meant to lead to engineering correlations to be used for more general optimization studies, essentially involving energy conservation and hence economic considerations.

(2) To determine the flow patterns in the corrugated passages and the distribution of the local heat transfer coefficient on the heat exchange surface (and their dependence on the geometry and the operating conditions). This was meant to support the design of high-efficiency surfaces, for example by identifying 'hot' and 'cold' spots or regions of high wall shear stress and mechanical energy dissipation.

In order to restrict within feasible limits the potential range of parameters to be investigated, the study was initially focused on the so-called crossed-corrugated geometry, shown in Fig. 3 and fully described in the following section. It will be noted that this possesses a (simple) symmetry not apparent in the geometries of Fig. 2.

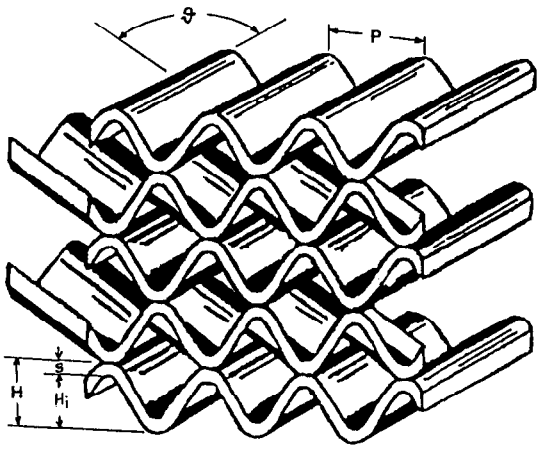

Fig. 3. Crossed-corrugated (CC) heat transfer elements.

Experimental work involved mainly local Nusselt number measurements by colour digital processing of liquid crystal images [liquid crystal thermography

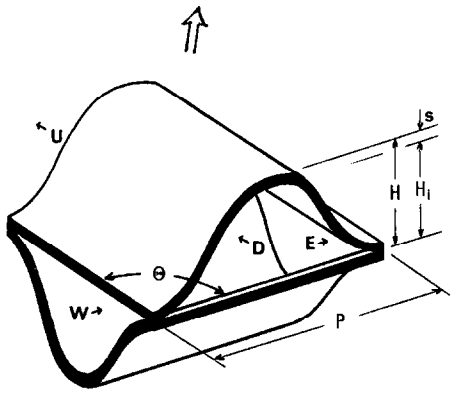

Fig. 4. Unitary cell (perspective view).

(LCT)]; wall pressure distributions were also measured by pressure tappings, and preliminary investigations of the flow field by particle-image velocimetry (PIV) were conducted. Numerical work was based mainly on three-dimensional simulations using the AEA code FLOW3D (Release 2) with various modifications and adaptions; simulations were conducted for laminar conditions and using different turbulence models (including direct and large-eddy simulations), and different boundary conditions were considered. Experimental and numerical results were critically compared and were also assessed against bulk performance data and laboratory results available from the literature.

The main results obtained by the authors have been documented in a series of confidential reports [7]; they have also been partially published, for example, in refs. [8, 9]. Here, we concentrate on the experimental technique and on typical results from a series of measurements relative to $P/H_i = 2.22$ to 4.00, $\theta = 30°$ to 79°, and Reynolds numbers in the range 500–5000. Numerical results are discussed in Part II [10].

1.2. *Corrugation geometry and performance parameters*

The geometry of the problem considered here (crossed-corrugated) is shown in Fig. 3. Closely packed plates, bearing sine-wave corrugations, delimit open flow passages which intersect one another at an angle θ; a complex flow and temperature field is established, which may result in high heat transfer rates with comparatively low pressure drops.

Although the exchangers themselves are substantial pieces of engineering equipment, they are composed of a very large number ($\sim 10^7$!) of nominally identical, small geometrical elements. For the crossed-corrugated design, a unitary cell can be identified as sketched in Fig. 4. It has two inlets (W, D) and two outlets (U, E) and its geometry is completely specified by the parameters P (pitch), H (external height), s (wall thickness) and θ (corrugation angle), all indicated in the figure. Other relevant geometrical quantities can be derived from these as summarized in Table 1.

The above geometrical correlations are based on the simplifying assumption of perfectly sinusoidal corrugations. The length L in Table 1 is then given by:

$$L = \frac{2E(\alpha, \pi/2)}{\pi \cos\alpha} P \tag{1}$$

in which E is the elliptic integral of the second kind:

$$E(\alpha, \phi) \equiv \int_0^{\phi} \sqrt{(1 - \sin^2\alpha \sin^2\phi')}\, \mathrm{d}\phi' \tag{2}$$

while the angle α is given by:

$$\alpha = \arcsin \frac{\pi H_i/P}{\sqrt{[1 + (\pi H_i/P)^2]}}. \tag{3}$$

If G is the mass flow rate crossing the unitary cell, the mean velocity can be defined as:

$$U \equiv \frac{G}{\rho A_c}. \tag{4}$$

It is also equal to the velocity of the fluid just upstream of the exchanger, divided by the 'porosity' of the latter, $V/(V + Ss)$. The Reynolds number can be based on this and on the hydraulic diameter D_{eq} (4 × volume/wall surface of the unitary cell):

$$Re \equiv \frac{UD_{eq}}{\nu}. \tag{5}$$

The most relevant performance parameters of the heat exchange matrix are the pressure drop per unit length and the heat transfer coefficient.

The pressure drop can be made dimensionless by defining the equivalent friction coefficient:

$$f \equiv \frac{|\Delta p| D_{eq}}{\rho \Delta a U^2/2} \tag{6}$$

in which Δa is the extent of the unitary cell along the main flow direction, see Fig. 4. As regards heat transfer, a local Nusselt number can be defined as:

$$Nu \equiv \frac{q_w D_{eq}}{\lambda_f (T_w - T_f)} \tag{7}$$

in which q_w is the local wall heat flux, T_w is the local wall temperature, T_f is the average (mixing) fluid temperature and λ_f is the thermal conductivity of the fluid. Of importance is also the mean Nusselt number, which characterizes the overall heat transfer effectiveness of the exchanger. It can be defined in two different ways, i.e. either as:

$$\langle Nu \rangle \equiv \frac{1}{S} \int_S Nu\, \mathrm{d}S \tag{8}$$

(S being the lateral surface of a unitary cell), or as:

$$Nu_{av} \equiv \frac{\langle q_w \rangle D_{eq}}{\lambda(\langle T_w \rangle - T_f)} \tag{9}$$

$\langle q_w \rangle$ and $\langle T_w \rangle$ being the surface-averaged wall heat flux and temperature, respectively. The second definition is more appropriate as an engineering performance parameter. However, the two definitions

Table 1. Main geometrical quantities

Quantity	Symbol	Expression
Internal height	H_i	H-s
Internal volume	V	$P^2H_i/\sin\theta$
Lateral surface	S	$2PL/\sin\theta$
Hydraulic diameter	D_{eq}	$4V/S$
Flow cross-section	A_c	$2PH_i \sin(\theta/2)/\sin\theta$
Inlet-to-outlet length	Δa	$P\cos(\theta/2)/\sin\theta$

coincide for a uniform wall temperature, a condition which is closely approximated both in real exchangers and in the laboratory tests.

1.3. *Literature review*

As mentioned in the Introduction, in the past the choice of geometry and Reynolds numbers for rotary air heaters was left largely to intuition and empiricism. Only a few experimental investigations have been presented in the literature for this or similar geometries, none of which includes detailed fluid flow data, and no previous three-dimensional numerical simulation is known to the authors.

In a pioneering paper, Savostin and Tikhonov [11] presented heat transfer and pressure drop results for Reynolds numbers ranging from 200 to 4000, corrugation angles θ from 0 to 144° and $P/H_i = 2.2$. Measurements were also taken for $\theta = 30°$ and P/H_i ranging from 0.8 to 2.3. The average heat transfer coefficient was determined by measuring the temperature variation of the air flowing across the test section, which was cooled by water and included about 10–20 unitary cells in the downstream direction. The authors observed that the Nusselt number increased significantly with θ, especially at Reynolds numbers above ~600 (for which they assumed that turbulent flow was established). The highest values of both Nu and f were attained for the highest values of P/H_i tested (~2), while heat transfer rates and hydraulic resistances decreased by ~15% as P/H_i decreased from ~2 to ~1. Correlations for f and Nu were proposed and were applied to an optimization study of a rotary regenerator. The authors concluded that—for given plate geometry, thermal power and overall frictional losses—increasing θ from 0 to 35–45° makes it possible to reduce significantly the heat transfer surface and depth of the exchanger, while keeping practically constant its front area; this results in a 30–40% saving in weight and cost. By increasing the corrugation angle further, even lower values are possible for the volume and heat transfer surface; however, due to the decrease of the allowable cross-sectional velocity (U), the front area increases sharply.

Focke *et al.* [12] used an electrochemical mass transfer method, the 'diffusion-limited current' technique (DLCT), to determine local mass transfer coefficients in water for $P/H_i = 2$, $Re = 10^2$ to 10^5, and θ ranging from 0 (corrugations aligned with the main flow, giving rise to independent, parallel straight ducts of sinusoidal cross-section) to 180° (corrugations normal to the main flow). Wall pressure was also measured. The test section included several tens of unitary cells (practically fully developed flow). Mass transfer coefficients were reported as the average Colburn-j factor, $j \equiv Sh/(Re\ Sc^{1/2})$, Sh being the Sherwood number (analogue of Nu) and Sc the Schmidt number (analogue of Pr). The authors observed a monotonical rise of both f and j for corrugation angles θ increasing from 0 to about 160°. Beyond this value, f and j decreased slightly and presented a local minimum for $\theta = 180°$ (the conditions for $\theta = 180°$ are not unequivocally defined in general, as they depend on the phase shift between the lower and upper plates; this was zero in the above experiments). The observed rise was much more pronounced for pressure drop than for mass transfer; for example, for θ increasing from 30 to 160° f increased about 20–30 times, while j increased only 2–2.5 times (depending also on the Reynolds number). One of the most significant results of this study is the curves reporting the behaviour of f and j as functions of Re for various corrugation angles. For $\theta = 0$, transition from laminar to turbulent flow is clearly indicated by a steep increase in both f and j at $Re = 6000$–10 000. As θ increases, the change in f and j becomes progressively smoother and the corresponding transitional Re decreases; transition becomes imperceptible for $\theta > \sim 60°$.

Focke and Knibbe [13] used the electrode-activated pH method, with *o*-cresolphthalein as the indicator, to visualize flow patterns between cross-corrugated plates. The geometry was the same as in the above paper; the authors limited their study to low Reynolds numbers (~10–1000) and included the case of the two plates forming different angles with respect to the main flow direction.

Gaiser and Kottke [14–16] investigated the dependence of Nu and f on the corrugation angle θ (in the range ~60–160°) for pitch-to-height ratios P/H of 1.78–7.12 and a Reynolds number of 2000. Their test section included over 100 unitary cells, so that practically fully developed conditions were attained, and the working fluid was air. Local mass transfer coefficients were measured by using a chromochemical reaction between a reactant added in gaseous form to the air and a second one absorbed in wet paper coating one of the walls; they were then converted into values of Nu by using the analogy between mass and heat transfer. Pressure drops were also measured by wall

pressure tappings. The authors report distributions of the local heat (mass) transfer coefficient and plots of the average Nusselt number and of the equivalent friction coefficient as functions of θ. Under comparable conditions, values of f were in good agreement with those measured by Focke *et al.* [12] and other authors. No explicit comparison of Nusselt numbers was made.

Further results, relative to a much more limited range of the geometrical and flow parameters, have been published by Okada *et al.* [17], Rosenblad and Kullendorff [18] and Zogg [19] (the last dealing with triangular corrugations).

As can be seen from the above survey, the present study is the first one in which all the relevant parameters (Re, θ, and P/H_i) have been made to vary independently. On the other hand, the range of corrugation angles considered here is more narrow than in previous studies, since the present investigation was closely focused on the geometries of highest interest for industrial rotary air heaters.

2. EXPERIMENTAL METHOD

2.1. *Review of liquid crystal thermography*

Thermochromic liquid crystals modify incident white light and display colours whose wavelength is a function of temperature. They can be painted on a surface or suspended in a fluid and used to visualize temperature fields. Liquid crystals change in appearance over a narrow range of temperatures called the 'colour-play interval', centred around the nominal 'event temperature'; the displayed colour is red at the lower temperature margin of this interval and blue at the upper end, and changes smoothly between these extrema. Both the colour-play interval and the event temperature can be selected by adjusting the liquid crystal composition; materials are available with event temperatures from -30 to 115°C, and colour play bands from 0.5 to 20°C, although not all combinations are feasible. Three types of liquid crystals are recognized as smectic, nematic and cholesteric. The cholesteric and chiral-nematic are generally used for heat transfer investigations as they display brilliant colour changes in a useful range of temperatures and can be handled without undue hazard.

Pure liquid crystals are thick, viscous liquids, greasy and difficult to deal with under most laboratory conditions. Two approaches have been adopted to make their use more practical: (i) encapsulation in a gelatine-like material, forming nearly spherical particles from 10 to 30 μm in diameter which can then be used as the pigment for water-based paints that air-dry to a hard finish; and (ii) application of the unencapsulated material (unsealed liquids) on a clear plastic sheet which is then sealed on the back by a black coat to form a pre-packaged assembly that can be applied on surfaces.

Unencapsulated liquid crystals provide the most brilliant colours, though the perceived hue is significantly affected by viewing and lighting angles. Also, the calibration and brilliance may change over periods of days or weeks under exposure to ultraviolet light, or even abruptly under exposure to some hydrocarbon vapours and other chemicals. Encapsulated material is more stable in calibration and less sensitive to viewing and lighting angles, but does not show comparably intense colours.

Reviews of liquid crystal applications are given, for example, by Kasagi *et al.* [20] and Moffat [21]. Several investigations have used liquid crystals as temperature transducers in engineering heat transfer studies. Akino *et al.* [22] used a liquid crystal film as the display device in a non-contacting thermal image system. Kasagi *et al.* [23] compared alternative techniques of liquid crystal application for the measurement of heat transfer coefficients and used them to investigate the effects of wall conductivity on film cooling effectiveness. Simonich and Moffat [24] used a liquid crystal film on a thin, electrically heated sheet to look for Taylor–Görtler vortices on a concave wall in a water-channel study of boundary-layer heat transfer. They were also employed by Goldstein and co-workers [25, 26] to visualize the heat transfer coefficient distribution under impinging jets. Hippensteele *et al.* [27] started a program of liquid crystal application for heat transfer research in gas turbines at NASA-Lewis.

Liquid crystals have also been used in suspension form to visualize thermal fields in fluids. Tanaka [28] used them to visualize the temperature distribution in water with application to thermal storage tanks. Natural convection heat transfer was investigated by Akino *et al.* [22] suspending liquid crystals in silicon oil, and by Hiller and Kowalewski [29] using glycerol.

There are three broad classes of image interpretation techniques available: human observation, intensity-based image processing and true-colour image processing.

Human observers can interpret liquid crystal images by direct visual inspection of the test section, of colour photographs or of tape recorded video images, usually employing narrow-band paints (colour play interval $\leqslant 1$°C). The associated uncertainty is generally one-third of the band width, i.e. about 0.2–0.5°C [21].

The second method is based on narrow-band optical filters, through which equally coloured regions can be extracted. For example, Akino *et al.* [22] developed a multiple narrow-band spectral intensity interpreter using a set of 18 filters, with central wavelengths ranging from 100 to 750 nm and full-width at half maximum (FWHM) less than 10 nm. The resolution of this method is better than 0.2°C.

Finally, in the true-colour image processing method colour video information is displayed as a matrix of picture elements (pixels), each characterized by a unique brightness combination of red, green and blue light (RGB). The relative fractions of red, green and blue determine the perceived colour and can be treated as the independent variables representing the colour

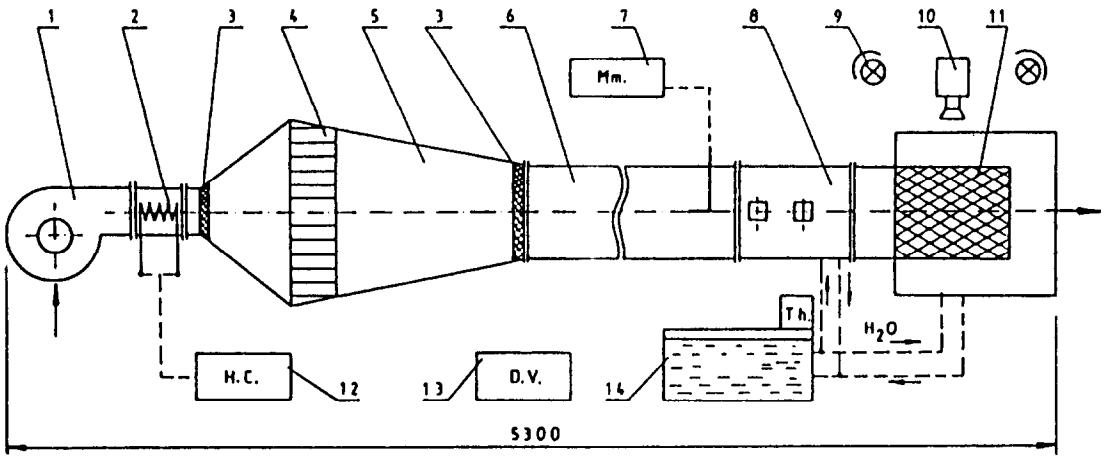

Fig. 5. Original design of the wind tunnel, including the fixed-geometry, small working section used in preliminary tests. (1) Fan; (2) heater; (3) screen; (4) honeycomb; (5) large settling chambers; (6) settling length; (7) micromanometer; (8) mapping section; (9) tungsten lamp; (10) camera; (11) working section; (12) heat controller; (13) digital voltmeter; (14) water bath.

numerically. The uncertainty of true-colour interpreters using wide-band liquid crystals is of the same order as the uncertainty resulting from human observers using narrow-band materials. It depends on the pixel-to-pixel uniformity of the applied paint and on the size of the area averaged by the interpreter.

2.2. *Experimental apparatus*

Experiments were carried out at the City University using an open, low-turbulence wind tunnel consisting of an entrance section with fan and heaters, settling chambers with diffusing screens and honeycomb, a mapping section (used for liquid crystal calibration and for parallel research) and a working section including the corrugated plates. The fan can give air flow rates corresponding to Reynolds numbers (in the corrugations) between 500 and 10^4, and the heaters can provide an air temperature, T_f, between 25 and 60°C.

The wind tunnel is shown schematically in Fig. 5; the small working section used for a preliminary series of measurements is also shown. It measured only 224×224 mm, included a limited number of unitary cells ('diamonds'), which did not allow fully developed flow and thermal conditions to be attained, and had a fixed geometry ($P/H_i = 3.34$, $\theta = 36°$). Besides wall heat transfer measurements, PIV was also attempted in this working section by Shand [30]; results, however, were disappointing due to reflections from the plastic walls and to difficulties in 'seeding' the air flow. The facility was successively modified by designing a new end portion, allowing for larger and more flexible working sections; this is shown in Fig. 6.

Each working section consisted of a pair of corrugated PVC plates having characteristic values of P and H (see Fig. 4). Corrugations were realized by shaping flat transparent PVC sheets, 0.75 mm in thickness, in a hot-water bath by means of a purpose-built device; they were about twice the scale of those in a typical rotary regenerator. Three geometries were investigated, whose basic parameters are summarized in Table 2. In all cases, the thickness s of the plates was 0.75 mm and the sinusoid length was 37 mm.

A typical arrangement of the working section is shown in Fig. 7. In the series of tests considered here, the plates were mounted at angles θ ranging from 30 to 79°. They include about six to seven unitary cells ('diamonds') streamwise and 10–12 spanwise; the circular test area, 300 mm in diameter, allows measurements up to six diamonds from entry, which correspond for all practical purposes to fully developed flow and thermal conditions. However, entry effects also can be investigated from diamonds 2 to 5–6 (see Section 3.3).

The working section voids into a larger rectangular box having a length of 700 mm and a cross-section of 80×570 mm. The lateral sides of the working section can be closed or left open; both conditions were tested as it was suspected that they could have an influence on the heat transfer and pressure drop results. In other published work [8–10] a closed-side boundary is employed, which means that the side flow is reflected back, thus affecting the overall flow patterns. On the other hand, when open boundaries are used the total flow rate through the working section may not be uniform streamwise, which in turn may lead to a departure from the 'ideal' behaviour. However, the condition of open side boundaries is thought to represent better the conditions prevailing in a real exchanger (periodic and 'infinite' array of cells), provided that the local flow rate is determined with some accuracy. Our experimental results have shown that closing the side boundaries has an appreciable influence only on the pressure drop, while heat transfer is little affected.

The top plate had its lower side (air side) coated by a liquid crystal sheet, while a uniform temperature T_b

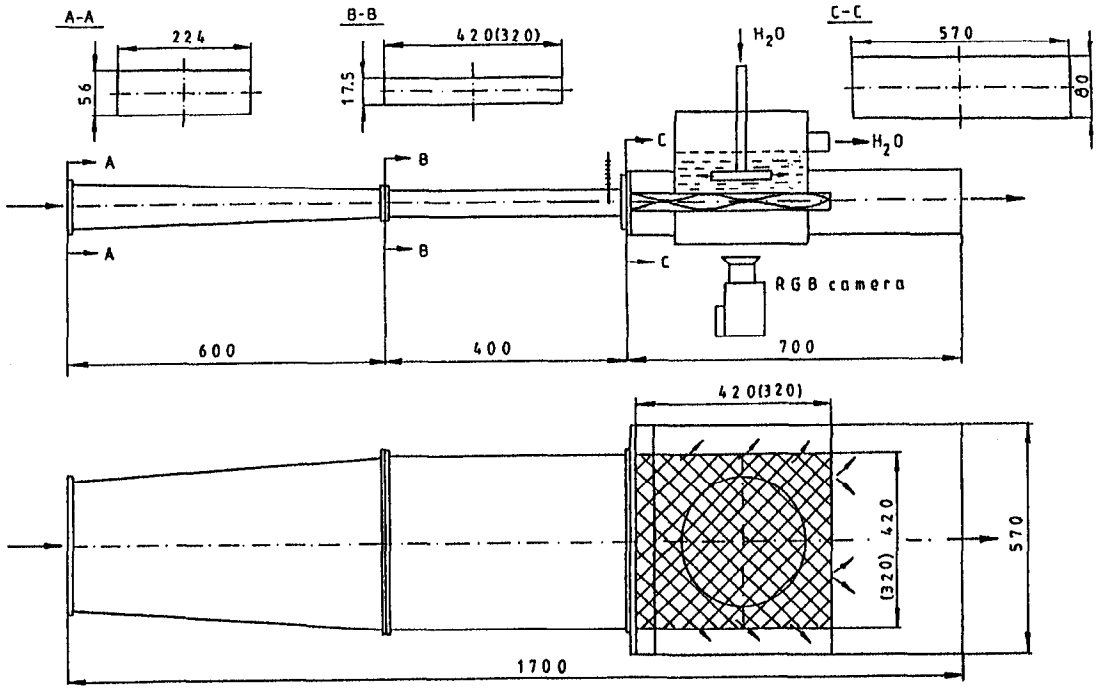

Fig. 6. New end portion of the wind tunnel, including the working section used for final measurements.

Table 2. Corrugation geometries

Geometry	A	B	C
P [mm]	32.00	29.50	25.00
H [mm]	8.75	10.40	12.10
H_i [mm]	8.00	9.65	11.35
D_{eq} [mm]	13.84	15.39	15.34
P/H	3.66	2.84	2.07
P/H_i	4.00	3.06	2.22

was provided on its upper side by a constant-temperature water bath (Fig. 6). With reference to Fig. 8, the local convective heat transfer coefficient on the air side, h, was computed from the known temperatures T_f (air) and T_b (water bath) and from the wall temperature T_w (indicated by the liquid crystal colour) using the following relation:

$$h = \frac{\lambda_t}{\delta_t} \frac{T_w - T_b}{T_f - T_w} \tag{10}$$

in which λ_t and δ_t are the average thermal conductivity and the total thickness of the corrugated plate (inclusive of the liquid crystal package). The Nusselt number was then obtained as $Nu = hD_{eq}/\lambda_f$. Equation (10) is valid assuming that lateral heat transfer by conduction along the wall is negligible compared with wall-to-fluid heat transfer; this assumption is satisfied well under the conditions studied. λ_t was independently determined by 'sandwiching' the PVC plate between thick aluminium walls, imposing a known power to an electric heater and measuring the total temperature drop.

The liquid crystals used here, manufactured in sheet form by Liquid Crystal Devices, had an event temperature range of 27.0–29.6°C. In the actual measurements, only the green colour band, corresponding to $T_w = 28.3 \pm 0.075$°C, was used as it is the brightest and sharpest. The air temperature T_f was kept fixed at about 45°C, and the temperature of the water bath was changed stepwise between 13 and 28°C; for each value of T_b, after steady-state conditions were reached, the colour pattern was recorded and analysed by an image-processing system. A series of contours of h, i.e. of the local Nusselt number, Nu, was thus obtained (one contour line for each T_b).

The image processing system (shown schematically in Fig. 9) included: an RGB video-camera; a PC 386 equipped with a 512 × 512 pixel, 8 bit (256 grey levels) Colour Frame Grabber board DT2871 and an Auxiliary Frame Processor DT2858 (produced by Data Translation); a 19 in colour display; and a colour laser printer. The video input section of the frame grabber incorporates a 10 MHz RGB/HSI converter for transforming in real time digitized pixel values representing weighted combinations of the primary colours (RGB) into new values representing hue, saturation and intensity (HSI). These can be subjected to a number of algorithms such as filtering, edge enhancement and averaging.

Mean Nusselt numbers $\langle Nu \rangle$ were computed as surface-weighted averages of Nu on a measurement cell by automatic analysis of the recorded images. The wall static pressure distribution was measured using pressure tappings, ~0.5 mm in diameter, located along the 'crests' and 'troughs' of the top corrugated

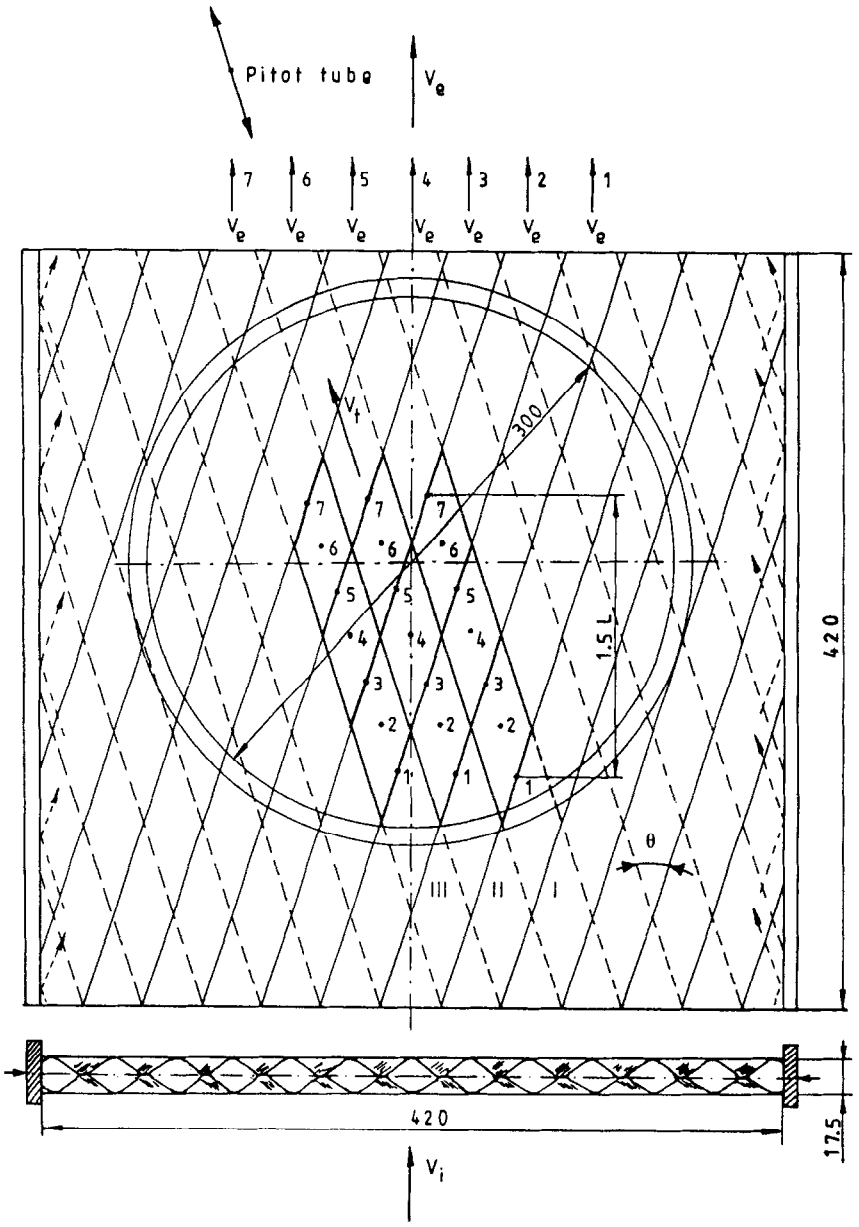

Fig. 7. Detail of the working section (angle $\theta = 36^\circ$, closed side boundaries).

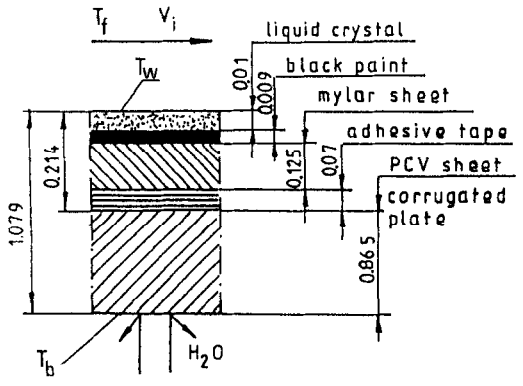

Fig. 8. Section of corrugated plate and liquid crystal package.

plate, in conjunction with a micromanometer. The equivalent friction coefficient f was computed by averaging over three consecutive cells. Both for $\langle Nu \rangle$ and f entrance effects were also studied.

The maximum air velocity along the corrugated passages between the plates, U_{peak}, was measured by a thin Pitot-static probe. The corresponding reference velocity U, used to compute the Reynolds number of the flow in the experiments and the friction coefficient f, equations (5) and (6), was expressed as:

$$U = \frac{U_{peak}}{F} \cos(\theta/2) \tag{11}$$

F being the peaking factor of the velocity distribution in each of the corrugated ducts. This, in turn, was

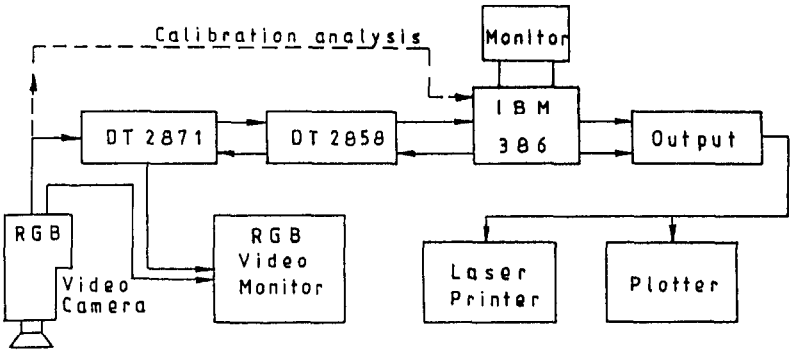

Fig. 9. Block diagram of the image-processing system.

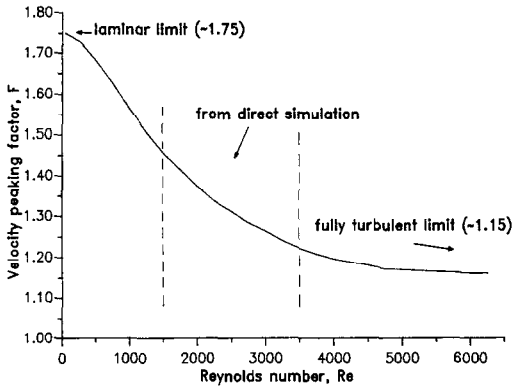

Fig. 10. Velocity peak factor F deduced from numerical simulations as a function of the Reynolds number.

deduced as a function of Re from high-accuracy numerical simulations [10]; for example, the function $F(Re)$ is reported in Fig. 10 for $\theta = 37°$ and $P/H_i = 4$. In the limit of small Reynolds numbers F takes the fully laminar value of ~ 1.75, and in the limit of large Re the fully turbulent value of ~ 1.15. In both limits, one must also have $dF/dRe = 0$. In the intermediate range $Re \approx 1500$–4000, results from direct turbulence simulations were used. Curves $F(Re)$ vary little with θ and P/H_i.

2.3. *Uncertainty analysis*

Recently, Moffat [31, 32] presented a general description of sources of errors in engineering measurements, of the relationship between error and uncertainty, and of the use of uncertainty analysis in the planning of an experiment. The uncertainty of a quantity R, which can be assumed to be a function of several variables $x_1 \ldots x_N$, can be estimated with good accuracy using a root-sum-square (RSS) combination:

$$\varepsilon_R = \left[\sum_{i=1}^{N}\left(\frac{\partial R}{\partial x_i}\varepsilon_i\right)^2\right]^{1/2} \tag{12}$$

ε_i being the uncertainty in the generic variable x_i. In this study, the heat transfer coefficient (or Nusselt number) was determined by using equation (10) as a function of a few independent variables. On the basis of equation (12), the experimental uncertainty in h can be calculated as:

$$\frac{\varepsilon_h}{h} = \frac{1}{h}\left[\sum_{i=1}^{N}\left(\frac{\partial h}{\partial x_i}\varepsilon_i\right)^2\right]^{1/2}. \tag{13}$$

As noted earlier, contours of h are not directly equivalent to isotherms, as measured from photographic or video images. Rather, they are determined after taking into account thermal conduction in the plate components for the two wall temperatures T_w and T_b, the bulk air temperature T_f, radiation from the lamps and other corrections. Lateral heat conduction in the corrugated plate is typically just 1.4% of the nett flux for $Re = 5000$. The maximum error in the measurement of the wall temperature T_w by the present method is $\pm 0.075°C$ (hue range 55–70). The error on the bulk air temperature T_f is $\pm 0.1°C$ and that on the water bath temperature T_b is $\pm 0.025°C$. The uncertainty in the thermal conductivity of corrugated plate plus liquid crystal package is within $\pm 0.005\ W\ m^{-1}\ K^{-1}$.

An example of the uncertainty analysis based on equation (13) is given in Table 3. It shows that at $Re = 5000$ the uncertainty in the local heat transfer coefficient h varies from $\pm 19\%$ (regions of minimum h) and $\pm 5.4\%$ (regions of maximum h). The uncertainty on the average heat transfer coefficient $\langle h \rangle$ is about $\pm 11\%$. Larger uncertainties occur at lower Reynolds numbers.

Since the largest uncertainties are associated with regions where the temperature difference between the liquid crystals (T_w) and the water bath (T_b) is small, some improvement over the present experimental accuracy could be achieved by significantly increasing the thickness s of the corrugated plate; this, however, would cause the experimental conditions to depart significantly from uniform wall temperature, which is closest to the operating conditions of real rotary air preheaters.

The uncertainty in the peak velocity U_{peak} along the corrugated ducts is within a few per cent due to measurement errors of the Pitot-static probe and micromanometer. Since the 'reference' velocity U is deduced from U_{peak} using equation (11) and the values of F in Fig. 10, an additional error is inevitably intro-

Table 3. Uncertainty analysis for $Re = 5000$, $\theta = 75°$, $P/H_i = 4.00$

x_i	λ_t [W m^{-1}K^{-1}]	δ_t [m]	T_b [K]	T_w [K]	T_f [K]	ε_h/h	
ε_i	0.005	0.025×10^{-3}	0.025	0.075	0.100		
$\lvert\partial h/\partial x_i\rvert$	209	36.5×10^{3}	256	12.4	2.09	0.190	(min. h)
$\lvert\partial h/\partial x_i\rvert$	710	124×10^{3}	171	17.4	7.10	0.054	(max. h)

duced in the Reynolds number Re, equation (5); this can be estimated to be within $\pm 5\%$ but, however, should not be strictly regarded as an experimental uncertainty. Finally, minor uncertainties in Re arise from irregularities in the channel spacing and from approximations in the physical properties of air. Of course, uncertainties in U cause corresponding uncertainties in the friction coefficient f, defined by equation (6); these can be estimated to be within $\pm 10\%$ under most conditions.

3. RESULTS AND DISCUSSION

3.1. *Heat transfer*

Typical overall heat transfer results are presented in Fig. 11; the average Nusselt number $\langle Nu \rangle$ is reported as a function of the Reynolds number for $P/H_i = 4.00$ and for two corrugation angles θ tested (60 and 75°). The Reynolds number-dependence of $\langle Nu \rangle$ is roughly described for all angles and pitch-to-height ratios by a 2/3-power law:

$$\langle Nu \rangle \approx Re^{2/3}. \tag{14}$$

Best-fit lines having this slope have been drawn together with the experimental data in Fig. 11. The dependence of $\langle Nu \rangle$ on Re is intermediate between the (theoretically) constant value that would be obtained in purely laminar flow, and the 0.8-power law typical of fully turbulent flows. The exponent 2/3 is also typical of transitional and turbulent flows with separation and reattachment [33].

The angle-dependence of $\langle Nu \rangle$ in the range $\theta = 45$–90° is evidenced in Fig. 12; experimental values of $\langle Nu \rangle$ are reported for two values of P/H_i investigated (3.06 and 4) and for $Re = 1000$ and 4000. Values of $\langle Nu \rangle$ for Reynolds numbers not coinciding with the experimental data were interpolated from the nearest results. The sensitivity of the Nusselt number to the angle between the corrugations seems to be slightly geometry-dependent; however, as a crude approximation, the θ dependence of $\langle Nu \rangle$ can be approximated by the simple exponential law:

$$\langle Nu \rangle \approx \exp(\theta/50°) \tag{15}$$

also reported in Fig. 12.

Finally, the dependence of $\langle Nu \rangle$ on the pitch-to-height ratio is shown in Fig. 13 for two different Reyn-

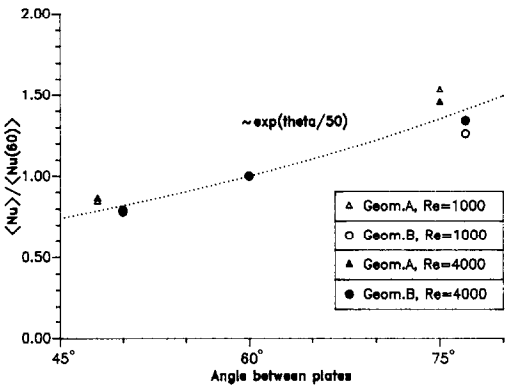

Fig. 12. Dependence of the average Nusselt number $\langle Nu \rangle$ on the corrugation angle θ for different values of Re and P/H_i. Dotted line: $\langle Nu \rangle \approx \exp(\theta/50°)$; symbols: experimental data.

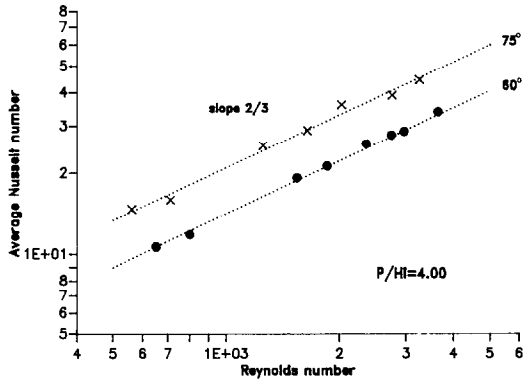

Fig. 11. Average Nusselt number as a function of the Reynolds number for two corrugation angles θ studied and $P/H_i = 4.00$. Lines having a slope of 2/3 have also been drawn.

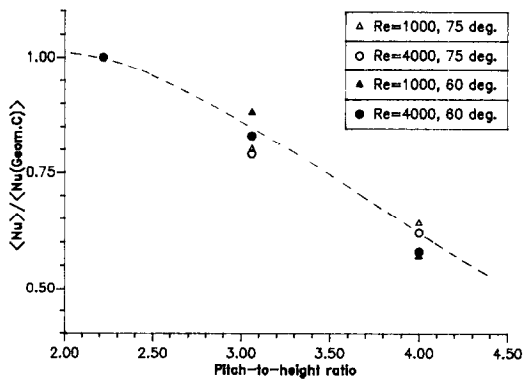

Fig. 13. Dependence of the average Nusselt number $\langle Nu \rangle$ on the pitch-to-height ratio P/H_i for different values of Re and θ. Values of $\langle Nu \rangle$ are normalized by those for geometry C ($P/H_i = 2.22$).

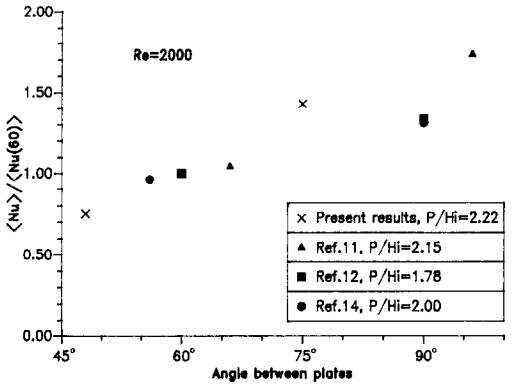

Fig. 14. Average Nusselt number: comparison of present results with literature data for $Re = 2000$. Values of $\langle Nu \rangle$ are normalized by those for $\theta = 60°$.

olds numbers and two angles. For given Re and θ, in the relatively narrow range investigated $\langle Nu \rangle$ is a decreasing function of P/H_i.

The Nusselt number results for $P/H_i = 2.22$ and $Re = 2000$ (interpolated from the nearest experimental points) are compared in Fig. 14 with literature results for closely similar geometries and the same Reynolds number. Values of $\langle Nu \rangle$ are normalized by those for $\theta = 60°$. The available experimental points are too sparse to allow a thorough comparison of the respective angle dependencies of the various sets. However, the present results seem to exhibit a slightly more marked increase with θ than previous measurements.

As regards the absolute levels of $\langle Nu \rangle$, at moderate corrugation angles ($\leqslant 60°$) the present values are slightly higher than those measured by Focke *et al.* [12] and by Gaiser and Kottke [14]. Larger discrepancies are found at larger angles. The experimental results of Savostin and Tikhonov [11] fall markedly below the present values.

The distribution of the local Nusselt number on the top (active) wall for $P/H_i = 4$ is shown in Fig. 15 for $\theta = 37°$, $Re = 2450$ (graph a) and for $\theta = 60°$, $Re = 3900$ (graph b). Note that the two graphs are not drawn to the same scale.

In both cases, maxima of Nu are attained near the downstream end of the trailing edge (on the right in the figure, also compare with Fig. 4). A secondary maximum is visible near the centre of the same edge, and high values of Nu are attained also in a narrow stripe of the leading (left) edge. The left and right edges of the diamonds shown in Fig. 15 correspond to sections of minimum cross-sectional area as seen by the fluid flowing (from left to right) in the bottom corrugation. They are also the regions of the top wall closest to the midplane of the unitary cell, where, as suggested by direct numerical simulations [10], the interaction between the two fluid streams flowing in the top and bottom conjugate ducts generates the highest levels of turbulence and mixing.

On the other hand, in the whole central ('furrow') region levels of Nu are quite low. This shows that this region contributes little to overall heat transfer, and supports the conclusion of Savostin and Tikhonov [11] that increasing the depth of the furrows beyond a certain limit, close to one half the corrugation pitch, causes a decrease in the average heat transfer coefficient.

As expected, minima of Nu are located around the four corners where the top plate touches the bottom one. The distribution of Nu becomes slightly flatter with increasing θ. The maps in Fig. 4 exhibit a satisfactory double periodicity along the left–right and up–down directions, confirming that conditions close to the fully developed state are actually attained in the measurement cell.

3.2. *Pressure drop*

Typical pressure drop measurements are reported in Fig. 16; the equivalent friction coefficient f is reported as a function of the Reynolds number for two different corrugation angles tested (60 and 75°) and for $P/H_i = 4.00$. The experimental data suggest a transitional behaviour, with a relatively marked rise of the f values as Re exceeds a transition value decreasing from ~ 2000 ($\theta = 60°$) to ~ 1000 ($\theta = 75°$). The slope of the curves, however, does not change appreciably and the Re dependence of f is roughly represented at all angles and pitch-to-height ratios by:

$$f \approx Re^{-1/2}. \tag{16}$$

Corresponding best-fit lines having this slope have been drawn together with the experimental data in Fig. 16.

The dependence of the friction coefficient upon the corrugation angle θ is shown typically in Fig. 17 for two values of P/H_i (3.06 and 4) and Re (1000 and 4000). As for $\langle Nu \rangle$ in Fig. 12, values of f for Reynolds numbers not coinciding with the experimental values were interpolated between the nearest available results. The dependence of f on θ can be crudely approximated at all Reynolds numbers and pitch-to-height ratios by a simple exponential law:

$$f \approx \exp(\theta/20°). \tag{17}$$

Clearly, the influence of the corrugation angle on the friction coefficient is much larger than on the Nusselt number, equation (15); for example, when θ increases from 60 to 75° $\langle Nu \rangle$ increases by only 30–40%, while f increases more than twice.

Finally, the dependence of f on the pitch-to-height ratio is difficult to separate from the influence of θ and Re. For example, values of f for two different Reynolds numbers (1000 and 4000) and angles (60 and 75°) are reported as functions of P/H_i in Fig. 18. The friction coefficient rises steeply for P/H_i increasing from ~ 2 to ~ 3 and is roughly constant, or even decreases, for further increases of the pitch-to-height ratio.

The present values of f for geometry C ($P/H_i = 2.22$) and $Re = 2000$ (interpolated from the

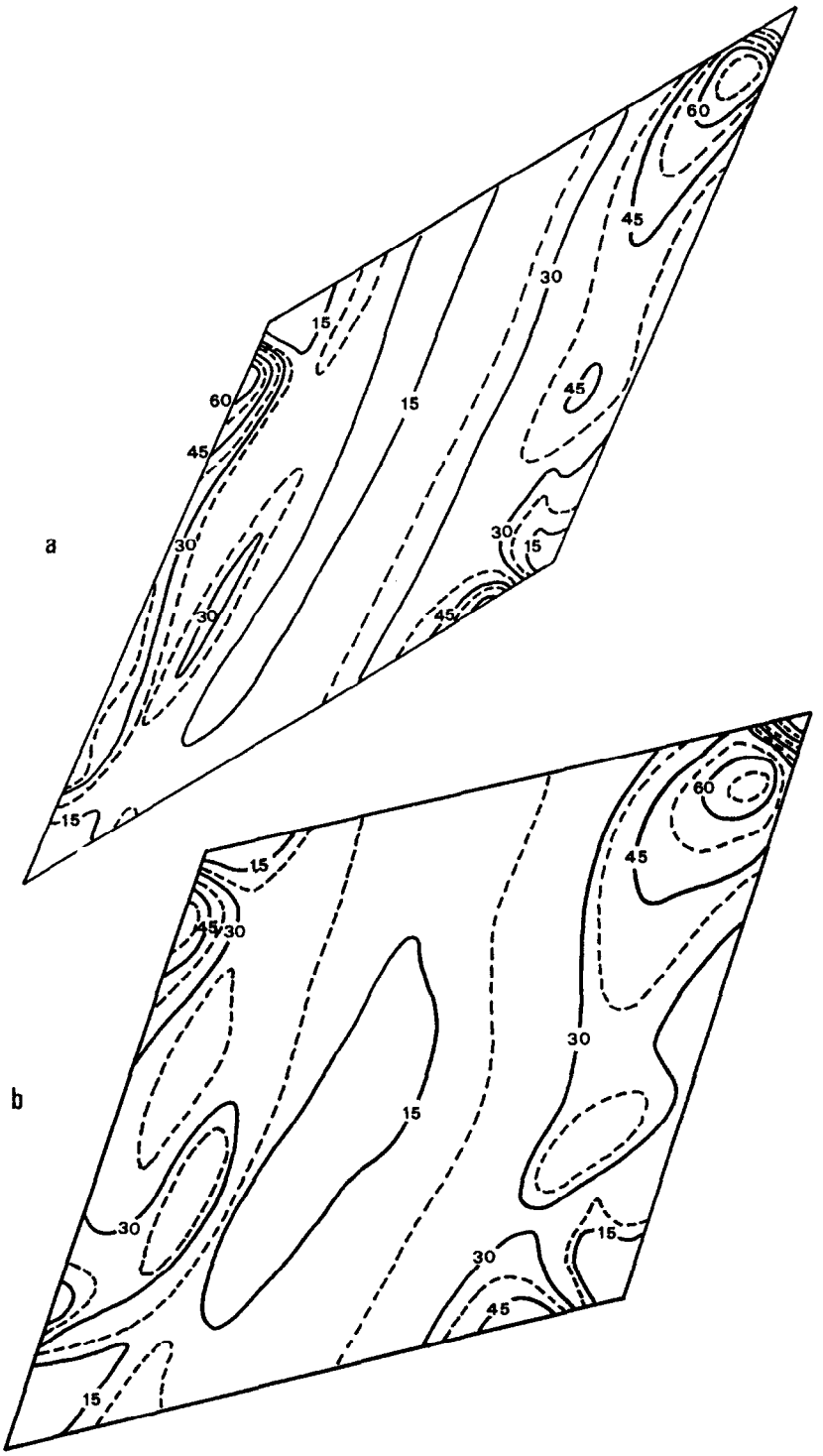

Fig. 15. Distribution of the local Nusselt number Nu on the top (active) wall. (a) $P/H_i = 4.00$, $\theta = 37°$, $Re = 2450$; (b) $P/H_i = 4.00$, $\theta = 60°$, $Re = 3900$.

nearest available experimental points and normalized by the value measured for $\theta = 60°$) are compared in Fig. 19 with literature results for similar geometries and the same Reynolds number. On the whole, the present results are in qualitative agreement with those measured by Savostin and Tikhonov [11], Focke *et al.*[12] and Gaiser and Kottke [14]; however, the angles investigated here are too few to allow definite

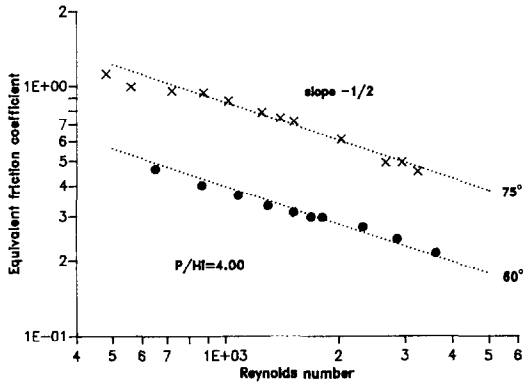

Fig. 16. Equivalent friction factor f as a function of the Reynolds number for two corrugation angles θ studied and $P/H_i = 4.00$. Lines having a slope of $-1/2$ have also been drawn.

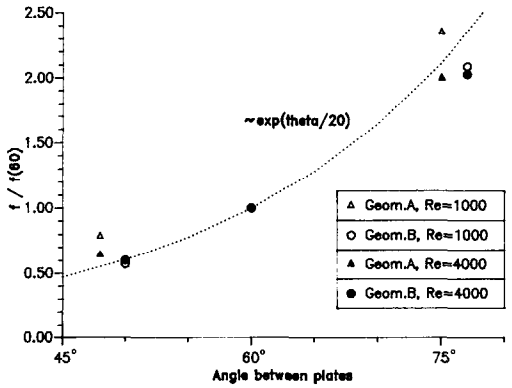

Fig. 17. Dependence of the equivalent friction factor f on the corrugation angle θ for different values of Re and P/H_i. Dotted line: $f \approx \exp(\theta/20°)$; symbols: experimental data.

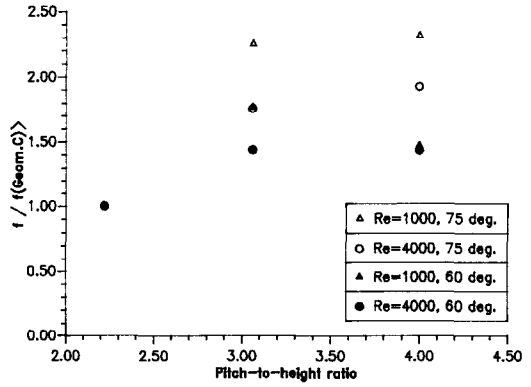

Fig. 18. Dependence of the equivalent friction factor f on the pitch-to-height ratio P/H_i for different values of Re and θ. Values of $\langle Nu \rangle$ are normalized by those for geometry C ($P/H_i = 2.22$).

conclusions, and the literature results themselves are rather sparse and scattered.

3.3. *Boundary and entry effects*

The values of Nu and f reported and discussed above are all for the condition of open side boundaries, which—as discussed in Section 2.2—is thought

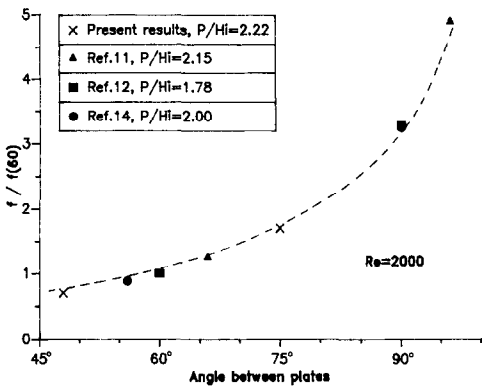

Fig. 19. Equivalent friction coefficient: comparison of present results with literature data for $Re = 2000$. Values of f are normalized by those for $\theta = 60°$.

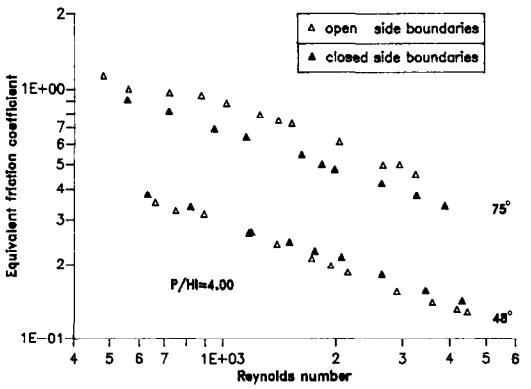

Fig. 20. Equivalent friction coefficient f as a function of Re for different angles and open or closed side boundaries (geometry A, $P/H_i = 4.00$).

to represent better the conditions prevailing in a real exchanger (~infinite array of cells).

The values of f measured as functions of Re and for different angles with open and closed side boundaries are compared in Fig. 20 for the aspect ratio $P/H_i = 4.00$ (geometry A). The main effect of closing the sides is a moderate decrease of the friction coefficient at the highest corrugation angle (75°); values of f for $\theta = 48°$ seem to increase slightly, but the effect is too small to be confidently separated from the measurement uncertainties. The influence of the side conditions on the Nusselt number was found to be negligible.

Entry effects can be appreciated by considering Fig. 21, which reports the average Nusselt number $\langle Nu \rangle$ (normalized by the corresponding fully developed value) measured in three consecutive cells of the test section for geometry C ($P/H_i = 2.22$), $\theta = 48°$ and different Reynolds numbers. These results show that entry effects can be quite significant, especially at the highest Re. However, they interest mainly the first two to three diamonds and can be assumed to have died out before the fifth diamond (Fig. 7), over which all the heat transfer measurements were taken. Similar remarks hold for the friction coefficient, f. Thus, the

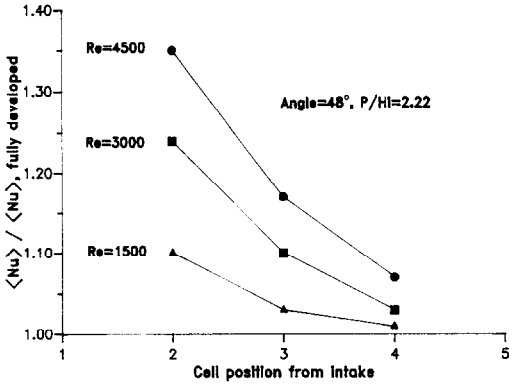

Fig. 21. Entrance effects: average Nusselt number $\langle Nu \rangle$ (normalized by the corresponding fully developed value) in consecutive cells for $\theta = 48°$, $P/H_i = 2.22$ and different Reynolds numbers.

measured values of $\langle Nu \rangle$ and f can be legitimately considered as representative of fully developed conditions.

4. CONCLUSIONS

This paper, together with Part II [10], reports the successful outcome of a comprehensive parallel experimental and predictive study of the problem of understanding the complex local flow and heat transfer patterns in the crossed-corrugated geometry. The effects of corrugation angle, geometry and Reynolds number have all been investigated. This is with a view to optimizing the design, as used in the very large rotary regenerators for conventional fuel power stations; however, the results are of interest to compact heat exchanger design generally. The local heat transfer has been measured using thermochromic liquid crystals combined with true-colour digital image processing. Part of the novelty is that flexible proprietary sheeting has been successfully applied to curved surfaces.

In the range investigated, the average Nusselt number $\langle Nu \rangle$ was found to increase approximately as $Re^{2/3}$ for all geometries; the typical effects on $\langle Nu \rangle$ of the corrugation angle and of the pitch-to-height ratio are also given. A comparison of the present results has been made with previous published data (particularly Savostin and Tikhonov [11]).

The equivalent friction coefficient f was found to decrease with the Reynolds number roughly as $Re^{-1/2}$. The angle dependence of f was much larger than that of the Nusselt number. The friction coefficient increased with P/H_i; an asymptote is suggested by the experimental data for $P/H_i > 4$.

Future work will involve applying the present methods to more complex and less symmetric geometric configurations, such as those shown in Fig. 2.

REFERENCES

1. W. M. Rohsenow, J. P. Hartnett and E. N. Ganic (Eds), *Handbook of Heat Transfer Applications* (2nd Edn), Chap. 4. McGraw-Hill, New York (1986).
2. B. Chojnowski and P. E. Chew, Getting the best out of rotary air heaters, *CEGB Res. J.* May, 14–21 (1978).
3. P. E. Chew, Rotary air preheaters on power station boilers, *Proceedings of the Symposium on Waste Heat Recovery and Utilisation*. Institute of Energy, U.K. (1985).
4. V. Nusselt, Die Theorie des Winderhitzers, *Z. Ver. Dt. Ing.* **71,** 85–91 (1927).
5. H. Hausen, *Warmeubertragung im Gegenstrom, Gleichstrom und Kreutzstrom* (2nd Edn). Springer, Berlin (1976).
6. A. J. Wilmott, The regenerative heat exchanger computer representation, *Int. J. Heat Mass Transfer* **12,** 997–1014 (1969).
7. Various authors, Local heat transfer and fluid flow fields in crossed corrugated geometrical elements for rotary heat exchangers, Report Nos 1–11, Thermofluids Engineering Research Centre, City University, London (October 1989–May 1992).
8. J. Stasiek and M. W. Collins, Liquid crystal mapping of local heat transfer in crossed corrugated geometrical elements for air heat exchangers, *Proceedings EUROTECH-Direct '91—Thermofluid Engineering*. Institution of Mechanical Engineers, U.K. (1991).
9. M. Ciofalo, G. Perrone, J. Stasiek and M. W. Collins, Numerical and experimental study of flow and heat transfer in cross-corrugated rotary regenerators, *Proceedings of the X National Heat Transfer Conference*, pp. 75–86. Unione Italiana di Termofluidodinamica, Italy (1992).
10. M. Ciofalo, J. Stasiek and M. W. Collins, Investigation of flow and heat transfer in corrugated passages—II. Numerical simulations, *Int. J. Heat Mass Transfer* **39,** 165–192 (1996).
11. A. F. Savostin and A. M. Tikhonov, Investigation of the characteristics of plate-type heating surfaces, *Teploenergetika* **17,** 75–78 (1970).
12. W. W. Focke, J. Zachariades and J. Olivier, The effect of the corrugation inclination angle on the thermohydraulic performances of plate heat exchangers, *Int. J. Heat Mass Transfer* **28,** 1469–1479 (1985).
13. W. W. Focke and P. G. Knibbe, Flow visualization in parallel-plate ducts with corrugated walls, *J. Fluid Mech.* **165,** 73–77 (1986).
14. G. Gaiser and V. Kottke, Flow phenomena and local heat and mass transfer in corrugated passages, *Chem. Engng Technol.* **12,** 400–405 (1989).
15. G. Gaiser and V. Kottke, Visualization of flow phenomena and local heat and mass transfer in corrugated passages. In *Flow Visualization* V (Edited by R. Reznicek), pp. 835–842. Hemisphere, New York (1990).
16. G. Gaiser and V. Kottke, Effects of corrugation parameters on local and integral heat transfer in plate heat exchangers and regenerators, *Proceedings of the Ninth International Heat Transfer Conference*, pp. 85–90. Hemisphere, Washington, DC (1990).
17. K. Okada, M. Ono, T. Tomimara, T. Okuma, H. Konno and S. Ohtani, Design and heat transfer characteristics of new plate heat exchanger, *Heat Transfer - Jap. Res.* **1,** 90–95 (1972).
18. G. Rosenblad and A. Kullendorff, Estimating heat transfer rates from mass transfer studies on plate heat exchanger surfaces, *Wärme-und Stoffübertratung* **8,** 187–191 (1975).
19. M. Zogg, Strömungs- und Stoffaustauschuntersuchungen der Sulzer Gewebepackung, Dissertation 4886, Eidgenössische Technische Hochschule, Zurich (1972).
20. N. Kasagi, R. J. Moffat and M. Hirata, Liquid crystals. In *Handbook of Flow Visualization* (Edited by W. J. Yang). Hemisphere, Washington, DC (1989).
21. R. J. Moffat, Experimental heat transfer, *Proceedings of the Ninth International Heat Transfer Conference*, pp. 187–205. Hemisphere, Washington, DC (1990).

22. N. Akino, T. Kunugi, K. Ichimiya, K. Mitsushiro and M. Ueda, Improved liquid crystal thermometry excluding human colour sensation, *ASME J. Heat Transfer* **111,** 558–565 (1989).
23. N. Kasagi, M. Hirata and M. Kumada, Studies of full-coverage film cooling: Part 1. Cooling effectiveness of thermally conductive wall, ASME Paper 81-GT-37 (1981).
24. J. C. Simonich and R. J. Moffat, New technique for mapping heat transfer coefficient contours, *Rev. Scient. Instrum.* **53,** 678–683 (1982).
25. R. J. Goldstein and J. F. Timmers, Visualisation of heat transfer from arrays of impinging jets, *Int. J. Heat Mass Transfer* **25,** 1857–1868 (1982).
26. R. J. Goldstein and M. E. Franchett, Heat transfer from a flat surface to an oblique impinging jet, *ASME J. Heat Transfer* **110,** 81–90 (1988).
27. S. A. Hippensteele, L. M. Russell and F. S. Stepka, Evaluation of a method for heat transfer measurements and thermal visualisation using a composite of a heater element and liquid crystals, *ASME J. Heat Transfer* **105,** 184–189 (1983).
28. T. Tanaka, Visualisation of the temperature field in thermal storage tanks by using the thermosensitive liquid crystal suspension method, *Proceedings of the International Symposium on Fluid Control, Measurement, Mechanics and Flow Visualisation* (*FLUCOME* '88), pp. 212–215. H. S. Stephens and Associates; sponsored by Sheffield University (1988).
29. W. J. Hiller and T. A. Kowalewski, Simultaneous measurement of temperature and velocity fields in thermal convective flows, *Proceedings of the fourth International Symposium on Flow Visualization* (Edited by C. Veret), Paris. Hemisphere, Washington, DC (1986).
30. A. M. Shand, Particle image velocimetry in a crossed corrugated acrylic Section, AEA-EE-0088, Harwell, U.K. (1990).
31. R. J. Moffat, Describing the uncertainties in experimental results, *Exp. Fluid Sci.* **1,** 3–17 (1988).
32. R. J. Moffat, Using uncertainty analysis in the planning of an experiment, *ASME J. Fluids Engng* **107,** 173–178 (1985).
33. M. Ciofalo and M. W. Collins, k–ε predictions of heat transfer in turbulent recirculating flows using an improved wall treatment, *Numer. Heat Transfer B* **15,** 21–47 (1989).